1.2

A Numerical Study on Convectively Induced Turbulence (CIT) Encounter above a Dissipating Deep Convection

Jung-Hoon Kim and Hye-Yeong Chun*

Department of Atmospheric Sciences, Yonsei University, Seoul, South Korea.

1. Introduction

Deep convection in the atmosphere is one of important sources for generating small-scale turbulent eddies (roughly 50 ~ 1000 m horizontal size) that can affect commercial aircraft. According to Kaplan et al. (2005), 86% of the severe turbulence events that caused human or structural damage in the United States from 1990 to 1996 occurred less than 100 km from the observed convective clouds. In the climatology of upper-level turbulence (> 20 000 ft) as recorded in pilot reports (PIREPs), approximately 20% of the turbulence over the United States (Wolff and Sharman 2009) and 11% over South Korea (Kim and Chun 2011) is related to deep convection, as identified by lightning flash data.

Convectively induced turbulence (hereafter CIT) is generally classified into one of two categories, depending on its location: in-cloud CIT and out-of-cloud CIT (Lester 1994). In-cloud CIT occurs in cloud boundaries due to strong variations in vertical velocity within the convective updraft. Although it is difficult to predict exactly the initiation and generation of individual convective cells using the operational numerical weather prediction (NWP) model with ~ 10 km horizontal grid spacing, pilots may easily avoid possible encounters with in-cloud CIT by detecting cloud boundaries visually and by observing on-board radar echoes. On the other hand, it is more difficult to identify the presence (generation, propagation, and dissipation) of out-of-cloud CIT, since it usually occurs in cloud-free or clear-air weather conditions.

As observational techniques and computational capacity have developed, several studies to understand out-of-cloud CIT have been conducted. Luce et al. (2010) used very high frequency (VHF) middle and upper (MU) atmosphere radar and lidar to observe clear-air turbulence (CAT) underneath cirrus clouds ahead of an accompanying warm front. Lenz et al. (2009) and Bedka et al. (2010) showed that convectively induced transverse bands and overshooting tops, detected by brightness temperatures (BTs) through the Infrared (IR) window channel of geostationary satellites (GEOS) with horizontal resolution of ~ 1 km, correlate highly with in situ turbulence data observed by commercial aircraft.

However, the spatial and temporal resolution of current observations still are not fine enough to understand the micro-scale phenomenon of out-of-cloud CIT. One feasible way to overcome this limitation is to investigate observed cases by using a high-resolution numerical model to simulate the entire evolving three-dimensional structure of a specific instance of turbulence, along with its

* *Corresponding author address*: Prof. Hye-Yeong Chun, Department of Atmospheric Sciences, Yonsei University, 262 Seongsanno, Seodaemun-gu, Seoul, 120-749, South Korea; E-mail: chunhy@yonsei.ac.kr

surrounding atmospheric conditions such as convections and large-scale flows. To do this, it is essential to simulate simultaneously the entire evolution of atmospheric flows at multi-scales, ranging from large-scale forcings to small-scale out-of-cloud CIT that may directly affect an aircraft.

Several studies have been performed using high-resolution numerical models to investigate the generation mechanisms of out-of-cloud CIT. In Lane et al. (2003), the Dickinson turbulence event that occurs above a developing convection was simulated in two- and three-dimensional numerical simulations with seven nested domains that reasonably reproduced not only the large scale flow, but also the out-of-cloud CIT. Lane et al. classified the generation mechanism for out-of-cloud CIT into two categories: i) convective and shearing instabilities above the developing convection, caused by convectively induced strong flow deformation and ii) subsequent breakdown of the convectively induced gravity waves after the initial overshooting tops. Given that in a two-dimensional framework the background zonal wind above the convection decreases with height (i.e., a negative wind shear condition), the wave propagating to the westward (i.e., in the down-shear direction) can break down when it approaches its critical level, at which the phase speed equals the background zonal wind, which finally leads to out-of-cloud CIT further above the convection. Lane and Sharman (2008) extended Lane et al. (2003)'s results to examine the effect of changing wind shear and static stability on gravity wave breaking above deep convection. Using a series of two- and three-dimensional ideal simulations, they showed that the altitude of the out-of-cloud CIT above the deep convection depends on the strength of the vertical wind shear (VWS) and the atmospheric stability above the deep convection. They suggested that additional sensitivity tests for directional wind shear and cloud properties, as well as other real-case simulations under various conditions, are still necessary to investigate the unexpected nature of out-of-cloud CIT.

Due to the potential severity of CIT, the Federal Aviation Administration (FAA) recommends in its avoidance guidance that an aircraft flying over a developing and/or mature thunderstorm should avoid cloud top by at least 1000 ft vertically for every 5 m s^{-1} of cloud-top wind speed (FAA 2008). Commercial airlines in Korea have similar guidelines to avoid CIT. For example, a commercial aircraft should climb to at least 5000 ft above cloud top when it passes over well-organized deep convection [personal communication with Captain Shin J.-S. (2008)]. However, it is still unclear whether such guidance allows an aircraft to avoid out-of-cloud CIT in all cases.

A particularly severe turbulence event occurred near convection en route from Jeju, Korea, to Osaka, Japan, at 1034 UTC 2 September 2007, which eventually caused six in-flight injuries. Unlike the case of Dickinson turbulence that occurred above a developing convection (Lane et al. 2003), this case likely occurred above a dissipating convection. The objective of this study is to document the detailed evolution of the observed turbulence along the deep convection and to investigate the generation mechanism of the turbulence based on numerical simulation. The Advanced Research Weather Research and Forecasting (ARW-WRF; Skamarock et al. 2008) model with six nested domains is used to simulate simultaneously multiple atmospheric conditions, ranging from large-scale flow to subsequent turbulence generation. Section 2 describes the investigation of the turbulence encounter and section 3 gives the experimental design of the ARW-WRF model. Section 4

compares the model results with available observations. Details of the convection evolution and the turbulence generation mechanism are investigated in section 5 based on the high-resolution simulation results. A summary and discussion are given in the last section.

2. Investigation of the turbulence encounter

On 2 September 2007, a commercial passenger aircraft (Airbus A300) en route from Jeju, Korea, to Osaka, Japan, encountered severe turbulence near Fukuoka at 33.68º N, 131.26º E (Fig. 1a). Figure 1b shows the flight altitude (ft) and vertical acceleration (1 g = 9.8 m s^{-2}) as a function of the flight time from 0956 UTC to 1115 UTC, obtained from the on-board digital flight recorder.

After the aircraft departed from Jeju at 0956 UTC, it ascended to its cruising altitude of 35 000 ft. At 1034 UTC, the aircraft suddenly experienced a 3-5 second period with strong variations in vertical acceleration, between +1.92 and -0.34 g. The maximum variation in vertical acceleration, 2.26 g, makes it a Category 6 turbulence (severe-extreme intensity of turbulence) based on the standard turbulence criteria of the International Civil Aviation Organization (ICAO) (Schwartz 1996). The reported cruising altitude of 35 000 ft at the incident time corresponds to an actual height of z = 11.2 km, computed by converting the pressure (241.7 hPa), as measured by the on-board barometer, to height, based on the standard atmospheric assumption (e.g., Lane et al. 2003; Kim and Chun 2010). After this incident, in which four passengers and two flight attendants suffered major or minor injuries, the aircraft changed its cruising altitude to 30 000 ft and eventually landed at Osaka at 1115 UTC. According to the pilots' statements, the impending severe turbulence gave no warning signs such as visually detectable deep convections or well-organized on-board radar echoes surrounding the aircraft [personal communication with Captains Shin J.-S. and Kim I.-G. (2008)].

To determine the existence of deep convection along the large-scale flow before the incident time, the evolution of BT around the turbulence location is examined at four different times (Fig. 2). Data in Fig. 2 comes from the IR channel of the Multifunctional Transport Satellite (MTSAT) with 4 km horizontal resolution data. Figure 2 also shows sea level pressure (SLP) at 0600 UTC, derived from the 6-hourly National Centers for Environmental Prediction/National Center for Atmospheric Research (NCEP/NCAR) reanalysis data with 1º × 1º horizontal grid spacing (Derber et al. 1991). As can be seen from the SLP at 0600 UTC, a low pressure system with the minimum SLP of 1001.28 hPa was located over the East Sea of Korea, and a cold front was elongated to the southwest into the Korea Strait. Ahead of this front, isolated deep convection appeared on the southwestern side of the turbulence location at 0730 UTC, about 3 hrs before the turbulence encounter (Fig. 2a). Under these synoptic circumstances, the pre-frontal trough on the warm-air side of the cold front provided the conditions necessary to develop the convection. As the convection moved northeastward, carried by the dominant southwesterly, it continued to develop until 0830 UTC (Fig. 2b). The convection then began diffusing and spreading horizontally (Fig. 2c) until 1030 UTC (Fig. 2d), demonstrating that the deep convection analyzed in this study was in the dissipating stage near the turbulence incident time and location.

To examine the evolution of the convection intensity quantitatively, the time series for the inverse of the minimum BTs found within the inner boxes (shown in Fig. 2) is depicted in Fig. 3, using the MTSAT data with 20-30 min time intervals. As shown in Fig. 3, there are two peaks in minimum

BT, one at 0810 (218.07 K) and the other at 0850 (216.91 K) UTC, indicating that the deep convection was in the developing and/or mature stage until 0900 UTC and further implying that the height of the cloud top increased abruptly due to the two overshooting tops within the deep convection. After 0900 UTC, the minimum BTs increased significantly to 224.65 K at 1000 UTC, indicating that the deep convection investigated in this study was a single-cell type. This also strongly suggests that the turbulence encounter at 1034 UTC 2 Sep 2007 was related to this deep convection while in the dissipating stage. In such conditions, it is likely that pilots near the dissipating convection would have had difficulty in detecting any indication of severe turbulence.

3. Experimental design of the model

The high-resolution numerical model used in this study is the ARW-WRF model version 3.1, was developed by the National Center for Atmospheric Research (NCAR) and released in April, 2009. This model is governed by non-hydrostatic and fully compressible prognostic equations on a grid structure of the Arakawa-C type. Detailed configurations of this model can be found in Skamarock et al. (2008). The ARW-WRF model has been used successfully for numerical weather prediction (NWP) and research. This model also has been used for studies on aviation turbulence (e.g., Feltz et al. 2009; Trier et al. 2009; Kim and Chun 2010).

Figure 4 shows the locations of the six nested domains considered in this study, with horizontal grid spacing of 30, 10, 3.3, 1.1, 0.37, and 0.12 km in domains 1, 2, 3, 4, 5, and 6, respectively. The locations of all domains are chosen to encompass the region of the turbulence encounter, as shown in Fig. 4b. To facilitate direct comparison of large-scale atmospheric conditions, domain 1 has the same horizontal grid spacing (Δx = 30 km) and extent (5730 km × 5130 km) as the analysis data from the Regional Data Assimilation and Prediction System (RDAPS) of the Korean Meteorological Administration (KMA). Model top is 20 hPa (about z = 27 km) with 113 vertical sigma layers. Vertical grid spacing in all domains decreases from 300 m at the surface to 100 m at z = 9 km, and then increases linearly from 100 m at z = 13 km to 500 m at the model top. Between z = 9 and 13 km, the vertical grid has a constant spacing of 100 m. In all domains, a sponge layer with Rayleigh damping is applied in the uppermost 5 km to prevent artificial reflections from the rigid upper boundary, and lateral boundary layers are specified with 5 relaxation grids. For initial and boundary conditions, the 6 hourly NCEP global final (FNL) reanalysis data with 1º × 1º horizontal grid spacings are used. The model was integrated for 18 hrs (00 UTC to 18 UTC 2 September 2007) in domains 1 and 2 and for 9 hrs (06 UTC to 15 UTC 2 September 2007) in domains 3, 4, 5, and 6. To simulate several scales of atmospheric flows simultaneously, two-way nesting interactions are con-ducted between domains 1-6 for 9 hrs (06 UTC to 15 UTC 2 September 2007) and between domains 1-2 for 18 hrs (00 UTC to 18 UTC 2 September 2007).

The physical parameterizations used in this study include the cloud microphysics scheme by Hong and Lim (2006), the land-surface scheme by Chen and Dudhia (2001), the short wave radiation scheme by Dudhia (1989), the long wave radiation scheme by Malwer et al. (1997), and the Mellor-Yamada-Janjić planetary boundary layer (MYJ PBL) scheme by Janjić (2002). The cumulus parameterization scheme by Kain (2004) is used only in domains 1 and 2. Note that the MYJ PBL scheme selected in this study takes into account the vertical mixings not only in the PBL but also in the free atmosphere by predicting subgrid-scale turbulent kinetic energy (SGS TKE). In the

selected PBL scheme, the non-zero SGS TKE is generated when the gradient Richardson number, Ri_g, is smaller than the critical value (0.505; Janjić 2002). Horizontal mixing is calculated using the Smagorinsky first-order closure scheme (Skamarock et al. 2008).

4. Comparison between the observations and model results

In this section, the large-scale features and deep convection simulated in the model are compared with those in the available observations, such as the RDAPS analysis data, radiosonde sounding data, and MTSAT imagery, to examine how the model reproduces the real atmosphere in the present case.

First, synoptic-scale flows assimilated in the 30-km RDAPS domain (Fig. 5, left) are compared with those simulated in the 30-km WRF model domain (domain 1; Fig. 5, right) at 1200 UTC 2 September 2007. Note that 1200 UTC is the closest time among the 12-hourly RDAPS analysis data to the incident time (1034 UTC). At the 300 hPa level (Fig. 5a), a highly curved upper-level trough with a jet stream of 48-50 m s^{-1} is located over the Korean peninsula. The trough moves eastward towards the incident region following the prevailing westerly. At the surface (Fig. 5b), a low pressure system, with a minimum SLP of 1001 hPa, is located over the East Sea of Korea, and its cold front is elongated to the Strait of Korea. The low pressure system is being strengthened as the upper-level trough approaches the surface frontal system. Figure 5 shows that the large-scale flow surrounding the turbulence region is fairly well reproduced in the WRF 30-km model domain.

However, some noticeable discrepancies exist in Fig. 5b between the simulation and RDAPS: (a) the SLP pattern at the western edge of the WRF 30 km domain (over the Tibetan plateau region near 30~35ºN, 100~105ºE) is less clear in the simulation, and (b) the ninth typhoon, 'Fitow', centered near 28ºN, 149ºE in the south-eastern part of the domain, is less intense in the simulation than the observations. The reduced typhoon intensity may be caused by the absence of a tropical cyclone (TC) bogus scheme during the model initialization process. These differences notwithstanding, upper-level large-scale flows (Fig. 5a) and SLP (Fig. 5b) near the turbulence region shown as asterisk in Fig. 5 seem not to be affected significantly by either the air flows over the Tibetan plateau or the typhoon 'Fitow'. As realistic simulation of the SLP over Tibetan plateau and/or the typhoon 'Fitow' is not the main purpose of this study, it is concluded that the simulation in the area of the turbulence is sufficient for present purposes.

Fukuoka, shown as a dot-circle in Fig. 4b, is the closest radiosonde station to the turbulence location. Figure 6 compares data from soundings (gray) taken at Fukuoka at 0600 UTC with simulation results in domain 1 (black), expressed as a conventional skew T-log *p* diagram. Note that the observed (far right) and simulated (right) wind barbs are also shown in the right side of Fig. 6. In the thermodynamic profile, a shallow inversion layer appears in the low troposphere at z = 1 km, location of the lifting condensation level (LCL). The convective available potential energy (CAPE) based on the observed data is about 1568 J kg^{-1}, sufficient to provide favorable conditions for well-developed convections. The tropopause height, defined as the lowest level at which the lapse rate is less than 2 ºC km^{-1} for a layer thicker than 2 km (WMO 1957), is located near z = 13.4 km. In the wind profile, a southwesterly flow dominates the entire troposphere and horizontal wind speed increases with height to z = 8 km, where the maximum wind speed is 17-20 m s^{-1}. Above z = 8

km, wind speed continually decreases to z = 16 km. The model captures the vertical features of the observed sounding fairly well, although with some discrepancies: i) local fluctuations in the observed profile of the dew-point temperature are not simulated accurately; ii) the simulated LCL (924 hPa level) is a little lower than the observed one (908 hPa level) due to the slightly stronger inversion in the low altitude in the simulation; (iii) as a result the CAPE in the simulation (1907 J kg^{-1}) is a little greater than the observation (1568 J kg^{-1}); and iv) the simulated maximum wind speed at z = 8 km (17 m s^{-1}) is slightly lower than the observed one (20 m s^{-1}).

Figure 7 compares the simulated deep convection with the observations at 1030 UTC 2 September 2007. Figure 7a shows the composite image of the MTSAT focused on the turbulence region, while Fig. 7b shows the column-maximum radar reflectivity (shading) and the SLP (contour) simulated in domain 2 (Δx = 10 km). At this time, simulated clouds align along the surface cold front that extends from the East Sea of Korea to the East China Sea through the Korea Strait (Fig. 7b), consistent with the observed clouds shown in Fig. 7a. Ahead of this front, isolated deep convection appears near the turbulence location in domain 2 (Fig. 7b), which is also similar to the observations (Fig. 7a). Although some local discrepancies in the convective structures are found in Fig. 7, the model results are in good agreement with the observations for the timing, location, and detailed structure of the simulated deep convection, as well as for the large-scale features surrounding the incident region. Therefore, the detailed evolution of the deep convection and the generation mechanism of the turbulence will be examined in the next section using the higher resolution domains of the present nested model.

5. Model results

a. Evolution of the deep convection

Figure 8 shows the horizontal evolution of the non-zero SGS TKE (shading) and cloud boundary (contours) in domain 4 (Δx = 1.1 km) at z = 11.2 km (the altitude of the turbulence encounter) for 2.5 hrs, from 0800 to 1030 UTC. For 1 hr, from 0800 to 0900 UTC, the deep convection (inner boxes in Fig. 8) is in the developing stage. During this time, the convection develops as a large mass of cloud in the troposphere, with three individual convective cells. At 0830 UTC, the first updraft of the convection reaches above z = 11.2 km, penetrating the tropopause (Fig. 8b). At 0900 UTC, two more updrafts penetrate above z = 11.2 km (Fig. 8c), while the first updraft has begun to spread out due to the divergent flows at the cloud top (Figs. 8 b and c). After 0900 UTC, the highly dense cloudy masses near the individual convective cells diffuse significantly, suggesting that the targeted deep convection has mostly dissipated by 1030 UTC (Figs. 8d-f). During this period, non-zero SGS TKE outside the cloud boundary begins to appear at z = 11.2 km (Figs. 8d-f), intersecting the flight route of the aircraft (Figs. 8e and f). At 1030 UTC, the simulated turbulence location is highly consistent with the actual location of the turbulence encounter (Fig. 8f).

To examine the quantitative intensity of the simulated deep convection, the time series of maximum vertical velocities within the inner boxes of Fig. 8 is shown in Fig. 9, using the model results in domain 4 with 10 min time intervals. According to this time series, the first peak of 33.13 m s^{-1} occurs at 0820 UTC, corresponding to the convective cell shown in Fig. 8b. The second peak of 33.1 m s^{-1} at 0850 UTC is due to the subsequent two cells shown in Fig. 8c. After 0850 UTC, the maximum vertical velocity decreases

significantly to 2.14 m s^{-1} by 1030 UTC (Fig. 9), implying that the targeted deep convection is in the dissipating stage at the incident time. The evolution of the maximum vertical velocity shown in Fig. 9, with two peaks in the developing stage and a significant decrease in the dissipating stage, correlates well with the time series for the observed minimum BT shown (Fig. 3). These correlations support the conclusion that the model aptly simulates the evolution of the observed deep convection.

b. Vertical evolution of the deep convection

Figure 10 shows vertical cross-sections of the total cloud mixing ratio greater than 0.05 g kg^{-1} and 0.1 g kg^{-1} (light and dark shading, respectively) and the potential temperature (contours) at selected times along the line shown in Fig. 8f, which is parallel to the direction of motion of the targeted deep convection. Figure 11 zooms in on the corresponding inner boxes in Fig. 10, showing vertical cross-sections of the cloud boundary (bold contour), potential temperature (contour), and SGS TKE greater (shading).

At 0800 UTC (Fig. 10a), the initial updraft of the convective cell is developing and deepening to about z = 8 km. Examining the enlarged cross-section at the cloud top region (Fig. 11a) shows that overturning isentropes due to the convective updrafts appear only in the cloud boundary. Vertical motion within the cloud is upward, and the flow out of the cloud is stable and smooth, with no evidence of instability. At 0830 UTC (Fig. 10b), this updraft penetrates the tropopause, located at about z = 13.4 km (see Fig. 6), and the cloud top reaches up to about z = 14.4 km. Due to this overshooting, gravity waves are generated and propagate upward to the stratosphere. Near the cloud top (Fig. 11b), the cloud boundary begins to overturn vertically with consequent vertical mixing, as shown by the non-zero SGS TKE near x = 30-34 km and z = 13.5-14 km. Considering that negative vertical velocity exists locally in this region (not shown), the vertical mixing is likely related to the entrainment process, in which unsaturated environmental air near the cloud top penetrates downward through the cloud boundary to mix with saturated cloudy air, which eventually leads to the dilution of the convective cloud top [e.g., Squires (1958), Klaassen and Clark (1985)]. Once this occurs, motion on the cloud top is no longer stable, as shown by some isentropes on the cloud top that are vertically overturned near z = 13.5-14 km in x = 10-15 km and x = 30-35 km in Fig. 11b. By 0900 UTC (Fig. 10c), the cloud top of the first updraft significantly decreases to about z = 12 km, while the second updraft (behind the first one) also penetrates the tropopause and then deepens to about z = 13.6 km. These two overshooting tops in the developing stage are consistent with the two peaks in the time series of the maximum vertical velocity described in Fig. 9.

In Fig. 11c, out-of-cloud CIT (identified by overturnings of isentropes with non-zero SGS TKE) is located about 1 km above the first convective cell, near z = 13-13.4 km and x = 42-48 km, while cloud thickness for both the first and second convective cells shrinks significantly (Fig. 10d) as the magnitude of upward motion decreases rapidly in the dissipating stage (Fig. 8). Because the convection during this period moves horizontally at about 11 m s^{-1} (80 km in 2 hr) and the zonal mean wind at 1000 UTC (Fig. 14f) decreases with height from 11 m s^{-1} at z = 9 km to 6 m s^{-1} at z = 11 km, the upstream regions (i.e., the left side) form the lee side of both convective turrets. For this reason, the dissipating convection cells tilt in the downshear direction (i.e., to the left) during the dissipating stage (Figs. 10d-f). In Fig. 11d, isentropes are relatively less compressed on

the lee side of the first updraft, near z = 10.5-11.5 km and x = 55 km. This indicates strong cloud-induced flow deformation and causes non-zero SGS TKE due to local shear instabilities (0 < Ri < 1) outside the cloud boundary. At 1000 UTC (Fig. 10e), the two cloud cells continue moving toward the turbulence encounter region and become more tilted in the downshear direction, with concurrent significant shrinking of their thicknesses. In Fig. 11e, localized shear instabilities with non-zero SGS TKE also appear on the lee side of the second convective cell, near z = 11.5-12 km and x = 50-57 km, consistent with previous studies regarding aircraft hazards on the lee side of the convection (e.g., Pantley and Lester 1990; Bedard and Cunningham 1991). By 1030 UTC (Fig. 10f), the entire cloud mass of the targeted deep convection has mostly disappeared. However, simulated non-zero SGS TKE outside the cloud still appears 1-2 km above the dissipating cloud, near z = 11-11.4 km and x = 86-96 km (Fig. 11f). At the incident time (1034 UTC), the location of the simulated non-zero SGS TKE closely coincides with the location of turbulence encounter (indicated by asterisk).

c. Generation mechanism of the turbulence

The previous section shows that the non-zero SGS TKE outside the cloud likely is related to two types of instabilities: (i) convective instability due to the entrainment of environmental air into the cloud and (ii) localized shear instability due to the cloud-induced flow deformation on the lee side of the convection. According to previous studies, upward motion in the convective cell and downward motion in the environment causes buoyancy gradients across the cloud interface that result in the production of y-vorticity according to the 2-D vorticity equation [$\partial\eta/\partial t \propto \partial B/\partial x$, where η and B are the y-vorticity ($\eta = \partial u/\partial z - \partial w/\partial z$) and buoyancy, respectively] (e.g., Klaassen and Clark 1985; Grabowski and Clark 1991; Lin 2007). When positive (negative) shear exists, convective cells or cumulus turrets tilt and stretch in the downshear (upshear) direction due to the shear-induced y-vorticity (e.g., Ackerman 1958; Grabowski and Clark 1993; Lin 2007). Finally, positive feedback between the production of y-vorticity and buoyancy gradients across the cloud interface leads to overturnings and vertical mixings at the cloud boundary through convective instability in the entrainment of environmental air into the cloud (e.g., Klaassen and Clark 1985; Grabowski and Clark 1991; 1993). With these factors in mind, the generation mechanism of the out-of-cloud CIT shown in Fig. 11f is examined in this section.

The simulated turbulence that passes through the incident region 1-2 km above the dissipating convection (Fig. 11f) is generated initially near the cloud boundary approximately 20 min before the incident time. To understand the excitation of the simulated turbulence, Fig. 12a shows the SGS TKE (shading), total cloud mixing ratio (contours), and horizontal wind vectors at z = 11.2 km, calculated using the model results in domain 5 (Δx = 0.37 km) at 1014 UTC. Derived using the model results in domain 6 (Δx = 0.12 km) at 1014 UTC, vertical cross-sections of horizontal wind speed (m s^{-1}), $\partial u/\partial z$ (s^{-1}), and SGS TKE (m^2 s^{-2}), taken along the blue line depicted in Fig. 12a, are shown in Figs. 12b, c, and d, respectively. Blue and black contours in Figs. 12b and c are y-vorticity (η; s^{-1}) and total cloud mixing ratio (0.03 and 0.1 g kg^{-1}), respectively. In Fig. 12d, zero N^2 (s^{-2}) is depicted as a blue contour (near x = 4 km and z = 11.2 km), and the total cloud mixing ratio of 0.3 g kg^{-1} and the isentrope of 346 K at 1012 (dashed) and 1014 (solid) UTC are shown as black and red lines,

respectively.

At 1014 UTC (Fig. 12a), a dominant south-westerly flow at the incident altitude is horizontally perturbed and distorted not only in the cloud but also on the lee side of the convection when it passes through the dissipating convection. At this time, non-zero SGS TKE appears at the leading edge of the dissipating cloud, which is the focus of the current study (Fig. 12a). Due to the horizontal disturbances in the cloud and on its lee side, the magnitude of the horizontal wind speed in the layer from z = 10-11.2 km is relatively smaller than the speed in the layers slightly above (z = 11.2-11.8 km) and below (z = 10 km) (Fig. 12b). Therefore, VWS above the dissipating convection is locally intensified in a layer from z = 11-11.6 km and x = 1-7 km, causing positive y-vorticity. In this region, the negative value of $\partial w / \partial x$ induced by the positive and negative vertical velocities in and out of the dissipating convection generates additional positive y-vorticity, although the magnitude of $\partial w / \partial x$ is much smaller than $\partial u / \partial z$ in this area, because the maximum vertical velocity of the dissipating convection at this time is small (see Fig. 9). Thus, the positive y-vorticity is nearly identical to the shear component of the y-vorticity ($\partial u / \partial z$) (Fig. 12c). In Figs. 12b and c, the leading edge of the cloud boundary begins to deform near z = 10.6-11.6 km and x = 4 km due to the shear-induced y-vorticity in this region (Fig. 12d). This cloud deformation is more pronounced at 1014 UTC than at 1012 UTC, which results in overturnings of isentropes (red contours) near the cloud interface at z = 11.2 km and x = 2-7 km (Fig. 12d). This finally activates turbulence and vertical mixing through convective instability in the entrainment of environmental air into the cloud across the cloud boundary (Fig. 12d). The generation mechanism for the turbulence at the leading edge of the dissipating convection elucidated in the current study is consistent with cloud interfacial instability (e.g., Klaassen and Clark 1985; Grabowski and Clark 1991; 1993).

To examine the evolution of the simulated turbulence, Fig. 13a (1014 UTC) shows the vertical cross-section of non-zero SGS TKE (shading), isentropes (contours), and the cloud boundary (blue bold contour). Figure 13b (1024 UTC) shows the Richardson number (shading), VWS (contours), and zero Brunt-Väisälä frequency (bold contour). Figures 13c and d show the same data, but at 1024 UTC, while Figs. 13e and f show the results for 1034 UTC. Figure 13 is taken along the blue line shown in Fig. 12a and uses model results from domain 6 (Δx = 0.12 km). Note that the vertical ranges in Fig. 12 and Fig. 13 are slightly different, although they are taken across the same horizontal distance.

For 20 min, from 1014 and 1034 UTC (Figs. 13a, c, and e), the turbulence generated at the cloud interface is advected by the dominant southwesterly flow, while the thickness of the dissipating convection shrinks continuously as the convection moves toward the observed turbulence encounter (shown as an asterisk). The turbulence caused by convective instability, near z = 11.2 km and x = 5-14 km, becomes wider and stronger at 1024 UTC (Figs. 13c and d) than at 1014 UTC (Figs. 13a and b), and finally comes out of the highly deformed cloud boundary in this region (Fig. 13c). By 1034 UTC, this turbulent region has continued to move horizontally, finally locating about 1-2 km above the dissipating convection. This eventually intersects the location of the observed turbulence (Figs. 13e and f). Assuming that the simulated results produced in this study are realistic, the severe turbulence encounter near Fukuoka at 1034 UTC 2 Sep 2007 was due to this out-of-cloud CIT. Also, even though only one case

was examined in this study, the very close agreement between simulation and observation strongly suggests that the aviation industry should consider out-of-cloud CIT above dissipating convection as an important inducer of CIT.

d. Subsequent breaking of the convectively induced gravity wave

This section describes the generation mechanism of the subsequent gravity wave breaking near *z* = 13 km and *x* = 12-20 km (Fig. 13a). To elucidate the evolution of the gravity waves and their breaking, Figs. 14a-c show vertical cross-sections with the same parameters as Fig. 13 (left), except taken at three earlier times. Figure 14d is the same as Fig. 13a, while Fig. 14e shows the space-time (*x*-*t*) cross-section of the vertical velocity (contour) at *z* = 12.5 km and the vertically averaged SGS TKE (shading) between *z* = 12.7 and 13.3 km in Figs. 14a-d. Figure 14f shows the vertical profile of the zonal-mean horizontal wind speed at 1000 UTC along the cross-section in Fig. 12a. Note that the *y*-axis in Fig. 14e is the time (min) since 0930 UTC. At 0956 UTC (Fig. 14a), phase lines of the gravity waves in *z* = 12.5-13.5 km and *x* = 0-10 km are tilted in the negative *x* direction, indicating upward propagation of gravity waves through the tropopause at *z* = 13.4 km and into the lower stratosphere. The waves with small horizontal wavelength (< 10 km) are initially generated by the first updraft near *z* = 10-12 km and *x* = 60-70 km at 0930 UTC, as shown in Fig. 11d. One wave starts to break down at 1000 UTC with non-zero SGS TKE at *z* = 13.3 km and *x* = 8 km (Fig. 14b). Once breaking begins to appear, it extends further downstream, following the motion of the dissipating convection (Figs. 14c and d). Eventually, the out-of-cloud CIT locates about 2 km further aloft (up to *z* = 13 km) above the dissipating convection of Fig. 13.

A vertically propagating gravity wave induced by deep convection can be a source of out-of-cloud CIT in the following ways. First, wave amplitude increases with height due to decreasing air density, which finally results in wave steepening and subsequent breaking at higher altitudes (Lindzen 1981). Second, an increase in atmos-pheric stability (*N*) near the tropopause can reduce the vertical wavelength (λ_z) of the wave accor-ding to the dispersion relationship for the two-dimensional internal gravity waves ($\lambda_z \propto |c-U|/N$, where *c* and *U* are the phase speed and background wind speed, respectively), which increases the potential for breaking (VanZandt and Fritts 1989). In a similar manner, vertically propagating waves will break or dissipate when they approach their critical level (z_c), at which the background wind speed equals the horizontal phase speed of the wave [$U(z_c) = c$]. As can be seen in Fig. 14e, the horizontal wavelength and phase speed of the waves is about 6-7 km and 3.2 m s^{-1} (tilted lines in Fig. 14e), respectively. Given the background wind condition shown in Fig. 14f, a wave with phase speed of 3.2 m s^{-1} meets its critical level at *z* = 13.6 km, depicted as a horizontal solid line in Fig. 14f, and it can break down at this time. The generation mechanism for convectively induced gravity wave breaking described in this study is consistent with Lane et al. (2003) and Lane and Sharman (2008), although the current study is focused primarily on the dissipating convection.

e. Resolution dependency of the simulated turbulence

To identify the resolution dependency of the simulated turbulence above the dissipating convection, vertical cross-sections of the SGS TKE, cloud boundary, and potential temperature in

different domains at 1030 UTC are depicted in Fig. 15, using the simulated results in domains 3-6 along the line shown in Fig. 12b. Overall features of the SGS TKE, potential temperature, and cloud boundary are similar in each domain. In particular, the region of simulated turbulence occurs in each domain with approximately the same and at the same location (about 1 km above the dissipating convection that directly passes through the observed turbulence at z = 11.2 km). This suggests that the numerical simulation with 3.3-km horizontal grid spacing is sufficient to identify the region of the out-of-cloud CIT in this case.

However, details such as the shape of the cloud, the overturning of isentropes, and the intensity of SGS TKE are somewhat different from each other. As expected, detailed cloud structures and small-scale motions are depicted in the high-resolution domains. In addition, overturning of the isentrope above the dissipating convection near z = 11.2 km and x = 14 km becomes clearer as the horizontal grid spacing decreases from domain 3 to domain 6. Therefore, the simulated maximum SGS TKE in this region ranges from 0.12 m^2 s^{-2} in domain 3 to 0.18 m^2 s^{-2} in domain 6. In addition, subsequent wave breakings near z = 13 km and x = 20 km in this cross-section appear only in domains 5 and 6, as these convectively induced gravity waves, with horizontal wavelengths of about 6-7 km, could not be resolved sufficiently in domains 3 and 4.

Current turbulence avoidance guidelines state that an aircraft flying over convection should avoid the cloud top by at least 1000 ft vertically for every 5 m s^{-1} of the cloud-top wind speed (FAA 2008). Since the wind speed at the cloud top altitude (z = 10 km) was about 10 m s^{-1} (Fig. 14f) at 1034 UTC, an aircraft following this guideline would need to move at least 2000 ft (about 0.7 km) above the cloud top. However, even if an aircraft followed this guideline in the situation investigated in this paper, it still would not gain sufficient clearance of the turbulence, because the out-of-cloud CIT is located about 1-2 km (3200 to 6400 ft) above the dissipating convection. Therefore, the deficiencies of the current turbulence avoidance guideline, highlighted by Lane and Sharman (2008), should be reconsidered not only for the developing stage of deep convection but also for the dissipating stage.

5. Summary and discussions

At 1034 UTC 2 Sep 2007, a commercial aircraft flying at its cruising altitude of 35 000 ft near Fukuoka and en route from Jeju, Korea, to Osaka, Japan, suddenly encountered severe turbulence (lasting only a few seconds), which caused six in-flight injuries. After landing, pilots stated that there were no pre-warning signals, such as developing thunderstorms or well-organized on-board radar echoes around the incident location and time. In observations, however, a deep convection ahead of the cold front developed in the southwestern region of the incident at 3 hr before the turbulence time. As this deep convection flowed with the dominant southwesterly towards the turbulence location, it entered into the dissipating stage, with a significant decrease of maximum BTs. Eventually, the convection passed through the turbulence location at the incident time, suggesting that the severe turbulence examined in this study is likely related to the dissipating convection.

We investigate the generation mechanism of the observed turbulence event using a high resolution numerical simulation. In this study, the WRF model, with six nested grid refinements (with the smallest grid spacing of 120 m), is used to reproduce the multi-scale atmospheric environments surrounding the turbulence. We find that the numerical simulations capture reasonably well the

observed large-scale flows and out-of-cloud CIT along the dissipating convection.

In the developing stage of the deep convection, an initial updraft penetrates the tropopause, and then subsequent updrafts appear behind the initial updraft. As the deep convection moves toward the turbulence location, the thickness of the convection shrinks significantly due to the rapid decrease of upward motion in the convection. In the dissipating stage, the dominant southwesterly flow at the aircraft's cruising altitude passes through the dissipating convection, and then it is disturbed significantly not only in the cloud but also on the lee side of the convection at 20 min before the incident time. This intensifies the local VWS on the lee side, which results in the production of positive *y*-vorticity. According to the 2-D vorticity equation, positive feedback between the production of *y*-vorticity and horizontal buoyancy gradients across the cloud boundary finally activates overturning and vertical mixing through convective instability at the cloud boundary in the entrainment of unsaturated environmental air into the cloud. While the dissipating convection with shrinking thickness continues to move toward the observed turbulence region, the turbulence generated at the cloud interface is advected by the dominant southwesterly flow and comes out of the convection, eventually locating 1-2 km above the dissipating convection and passing through the observed turbulence region at the incident time. Vertically propagating convective gravity waves with a phase speed of 3.2 m s^{-1} subsequently break down as they approach their critical level. In this situation, the out-of-cloud CIT locates further aloft, about 2 km above the dissipating convection. Even though only one case study is conducted here, currently used turbulence avoidance guidance (FAA 2008) should be reconsidered not only for the developing and/or mature stage of the deep convection, but also for the dissipating stage of the deep convection.

With respect to the resolution dependency of the simulated turbulence, the parameterized SGS TKE in a domain with horizontal grid spacing of 3.3 km is sufficient to identify the location of the out-of-cloud CIT at about 1-2 km above dissipating convection. As computer capacity relevant to numerical weather prediction (NWP) models has increased rapidly in recent history, the grid resolution of the operational NWP models has also increased. Locally focused high-resolution numerical modeling has successfully predicted observed turbulence cases, not only for complex mountains [e.g., Clark et al. (2000); Lane et al. (2009); Kim and Chun (2010)] but also for convective systems [e.g., Lane et al. (2003); Trier and Sharman (2009); and the present study]. Thus, NWP model-produced SGS TKE can be used to forecast aviation turbulence directly, and these results can be compared with currently used turbulence forecasting system [e.g., graphic turbulence guidance (GTG; Sharman et al. 2006)]. Considering that the forecasting performance of the *GTG* during the summer time over East Asia is relatively lower than in other seasons (Kim et al. 2011), the parameterized SGS TKE directly derived from an operational NWP model with higher grid resolution could help improve turbulence forecasts, at least when related to convective systems associated with large-scale flows over East Asia.

ACKNOWLEDGMENTS: This work was funded by the Korean Meteorological Administration Research and Development Program under Grant RACS_2011-8006.

REFERENCES

Bedard, A. J., Jr., and W. Cunningham, 1991: Potential aircraft hazards in the vicinity of

convective clouds: A review from the perspective of a scale-model study. Preprints, *Fourth Int. Conf. on Aviation Weather Systems*, Paris, France, Amer. Meteor. Soc., 66-70.

Bedka, K., J. Brunner, R. Dworak, W. Feltz, J. Otkin, and T. Greenward, 2010: Objective satellite-based detection of overshooting tops using Infrared window channel brightness temperature gradients. *J. Appl. Meteor. Climatol.*, **49**, 181-202.

Chen, F., and J. Dudhia, 2001: Coupling an advanced land surface/hydrology model with the Penn State-NCAR MM5 modeling system. *Mon. Wea. Rev.*, **129**, 569-585.

Clark, T. L., Hall, W. D., Kerr, R. M., Middleton, D., Radke, L., Ralph, F. Martin, Nieman, P. J., and D. Levinson, 2000: Origins of aircraft-damaging clear air turbulence during the 9 December 1992 Colorado downslope windstorm: Numerical simulations and comparison to observations. *J. Atmos. Sci.,* **57**, 1105-1131.

Derber, J. C., D. F. Parrish, and S. J. Lord, 1991: The global operational analysis system at the National Meteorological Center. *Wea. Forecasting*, **6**, 538-547.

Dudhia, J., 1989: Numerical study of convective observed during the winter monsoon experiment using a meso-scale two-dimen-sional model. *J. Atmos. Sci.*, **46**, 3077-3107.

FAA, cited 2008: Aeronautical information manual. Federal Aviation Administration, 670 pp. [Available online at http://www.faa.gov/airports_airtraffic/air_traffic/publications/media/aim.pdf].

Feltz, W. F., K. M. Bedka, J. A. Otkin, T. Grrenward, and S. A. Ackerman, 2009: Understanding satellite-observed mountain-wave signatures using high-resolution numerical model data. *Wea. Forecasting*, **24**, 76-86.

Grabowski, W. W., and T. L., Clark, 1991: Cloud-environment interface instability: Rising thermal calculations in two spatial dimensions. *J. Atmos. Sci.*, **48**, 527-546.

_____, and _____, 1993: Cloud-environment interface instability. Part II: Extension to three spatial dimensions. *J. Atmos. Sci.*, **50**, 555-573.

Hong, S.-Y., and J.-O. J. Lim, 2006: The WRF single-moment 6-class microphysics scheme (WSM6). *J. Korean Meteor. Soc.*, **42**, 129-151.

Janjic, Z. I., 2002: Nonsingular implementation of the Mellor-Yamada level 2.5 scheme in the NCEP Meso model. *NCEP office note*, No. 437, 61 pp.

Kain, J. S., 2004: The Kain-Fritsch convective parameterization: An update. *J. Appl. Meteor.*, **43**, 170-181.

Kaplan, M. L., A. W. Huffman, K. M. Lux, J. J. Charney, A. J. Riordan, and Y.-L. Lin, 2005: Characterizing the severe turbulence environments associated with commercial aviation accidents. Part 1: A 44-case study synoptic observational analyses. *Meteor. Atmos. Phys.*, **88**, 129-152.

Kim, J.-H., and H.-Y. Chun, 2010: A numerical study of clear-air turbulence (CAT) encounters over South Korea on 2 April 2007. *J. Appl. Meteor. Climatol.*, **49**, 2381-2403.

_____, and _____, 2011: Statistics and possible sources of aviation turbulence over South Korea. *J. Appl. Meteor. Climatol.*, **50**, 311-324.

_____, _____, R. D. Sharman, and T. L. Keller, 2011: Evaluations of upper-level turbulence diagnostics performance using the graphical turbulence guidance (GTG) system and pilot reports (PIREPs) over East Asia. *J.*

Appl. Meteor. Climatol., (In press).

Klaassen, G. P., and T. L. Clark, 1985: Dynamics of the cloud-environment interface and entrainment in small cumuli: two-dimensional simulations in the absence of ambient shear. *J. Atmos. Sci.*, **42**, 2621-2642.

Lane, T. P., R. D. Sharman, T. L. Clark, and H.-M. Hsu, 2003: An investigation of turbulence generation mechanisms above deep convection. *J. Atmos. Sci.*, **60**, 1297-1321.

_____, and _____, 2008: Some influences of background flow conditions on the generation of turbulence due to gravity wave breaking above deep convection. *J. Appl. Meteor. Climatol.*, **47**, 2777-2796.

_____, J. D. Doyle, R. D. Sharman, M. A. Shapiro, and C. D. Watson, 2009: Statistics and dynamics of aircraft encounters of turbulence over Greenland. *Mon. Wea. Rev.*, **137**, 2687-2702.

Lenz, A., K. M. Bedka, W. F. Feltz, and S. A. Ackerman, 2009: Convectively induced transverse band signatures in satellite imagery. *Wea. Forecasting*, **24**, 1362-1373.

Lester, P. F., 1994: *Turbulence: A New Perspective for Pilots*. Jeppesen Sanderson, 212 pp.

Lindzen, R. S., 1981: Turbulence and stress owing to gravity wave and tidal breakdown. *J. Geophys. Res.*, **86**, 9707-9714.

Luce, H., T. Nakamura, M. K. Yamamoto, and M. Yamamoto, 2010: MU radar and lidar observations of clear-air turbulence underneath cirrus. *Mon. Wea. Rev.*, **138**, 438-452.

Malwer, E. J., S. J. Taubman, P. D. Brown, M. J. Iacono, and S. A. Clough, 1997: Radiative transfer for in-homogeneous atmospheres: RRTM, a validated correlated-k model for the longwave. *J. Geophys. Res.*, **102**, 16663-16682.

Pantley, K. C., and P. F. Lester, 1990: Observation of severe turbulence near thunderstorm tops. *J. Appl. Meteor.*, **29**, 1171-1179.

Schwartz, B., 1996: The quantitative use of PIREPs in developing aviation weather guidance products. *Wea. Forecasting*, **11**, 372-384.

Sharman, R., C. Tebaldi, G. Wiener, and J. Wolff, 2006: An integrated approach to mid- and upper- level turbulence forecasting. *Wea. Forecasting*, **21**, 268-287.

Skamarock, W. C., J. B. Klemp, J. Dudhia, D. O. Gill, D. M. Barker, M. G. Duda, X.-Y. Huang, W. Wang, and J. G. Powers, 2008: A description of the advanced research WRF version 3. NCAR technical note, NCAR/TN-475+STR.

Squires, P., 1958: Penetrative downdraughts in cumuli. *Tellus*, **10**, 381-389.

Trier, S. B., and R. D. Sharman, 2009: Convection-permitting simulations of the environment supporting widespread turbulence within the upper-level outflow of a mesoscale convection system. *Mon. Wea. Rev.*, **137**, 1972-1990.

VanZandt, T. E., and D. C. Fritts, 1989: A theory of enhanced saturation of the gravity wave spectrum due to increases in atmospheric stabilitiy, *Pure Appl. Geophys.*, **130**, 399-420.

World Meteorological Organization (WMO), 1957: Definition of the tropopause. *WMO Bull.*, **6**, 136.

Wolff, J. K., and R. D. Sharman, 2008: Climatology of upper-level turbulence over the contiguous United States. *J. Appl. Meteor. Climatol.*, **47**, 2198-2214.

(a)

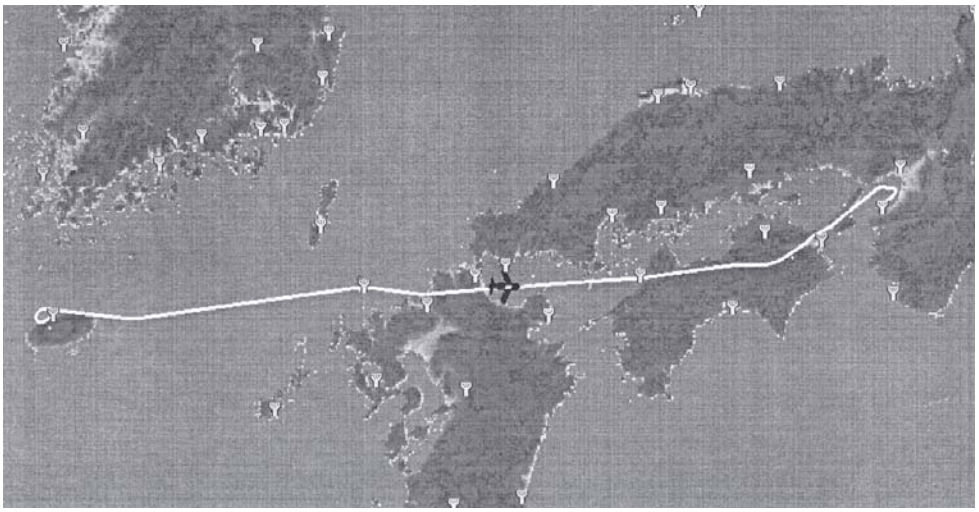

(b)

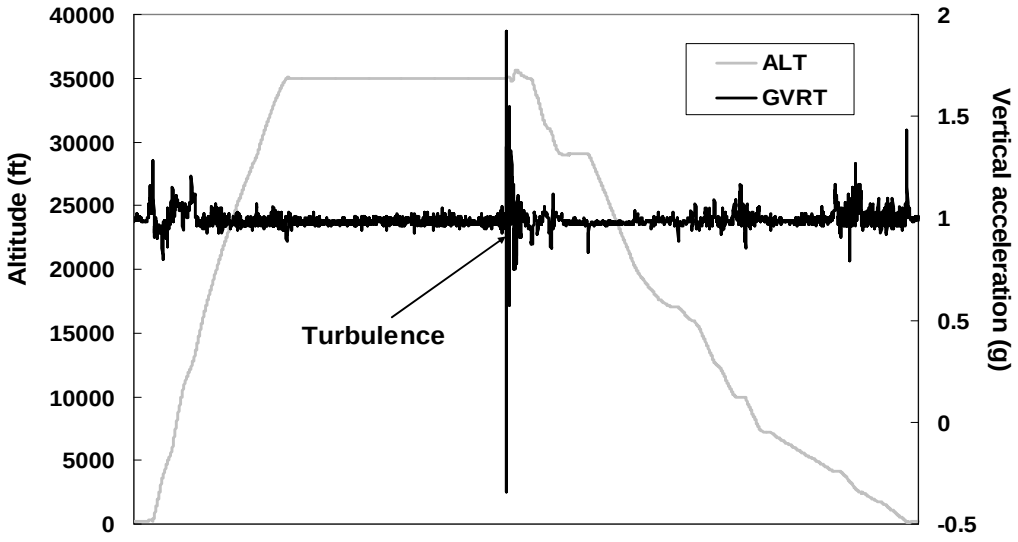

Fig. 1. The flight (a) route and (b) altitude (gray line) with vertical acceleration (m s^{-2}; black line) as a function of time from 0956 UTC (at Jeju, Korea) to 1115 UTC (at Osaka, Japan) on 2 Sep 2007, derived from the digital flight recorder (DFR) data with a 1-sec interval. Location (33.679ºN, 131.264ºE) and time (1034 UTC) of the turbulence encounter are depicted as a black aircraft in (a) and an arrow in (b), respectively.

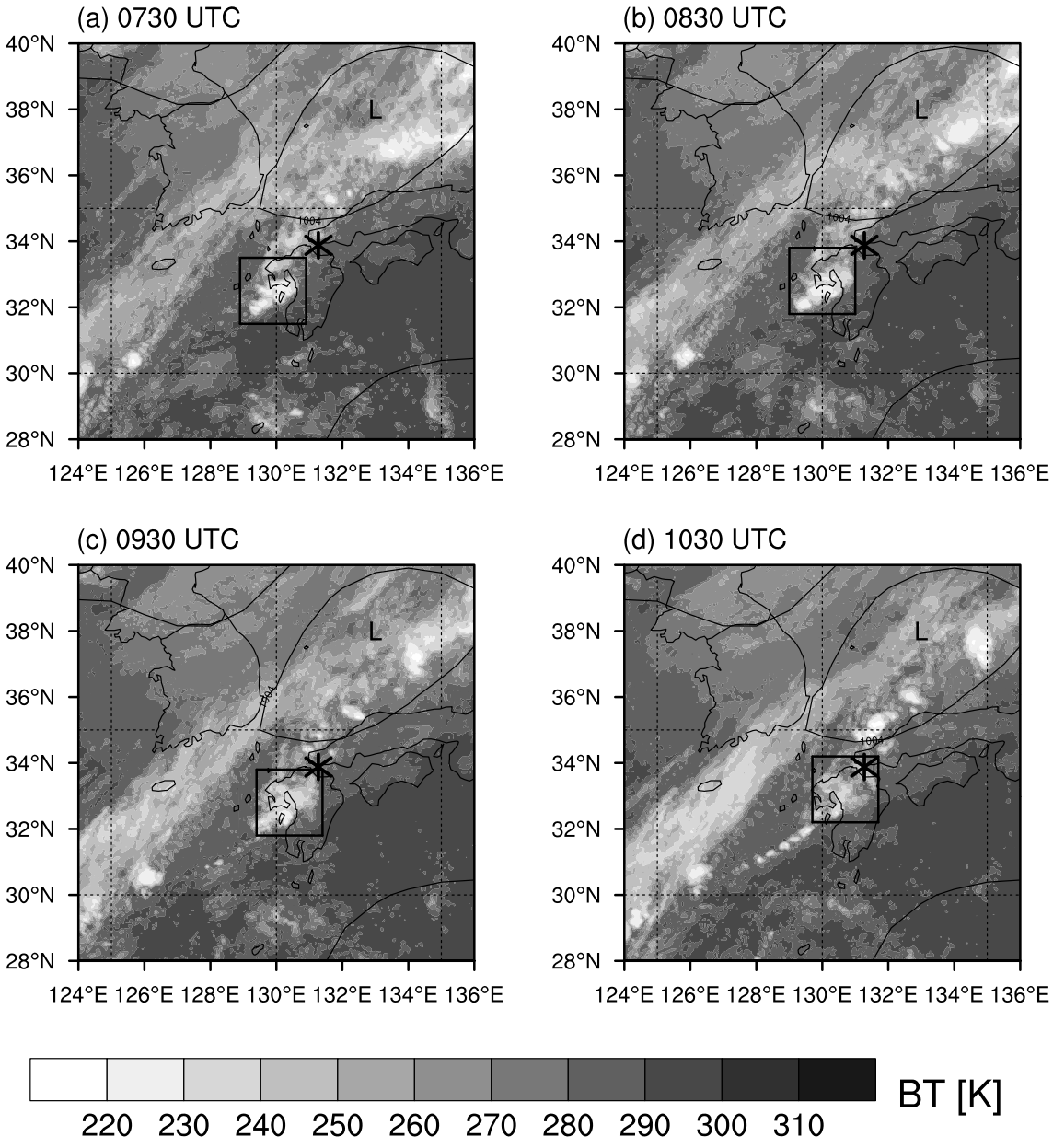

Fig. 2. Brightness temperature (shading) obtained from the MTSAT 4-km data at (a) 0733, (b) 0833, (c) 0933, and (d) 1033 UTC and sea level pressure (contours) derived from the NCEP/NCAR reanalysis data with 1º × 1º horizontal grid spacing at 0600 UTC 2 Sep 2007 over South Korea and western Japan. Contour intervals in all plots are 4 hPa and the location of the turbulence encounter is depicted as an asterisk in all plots.

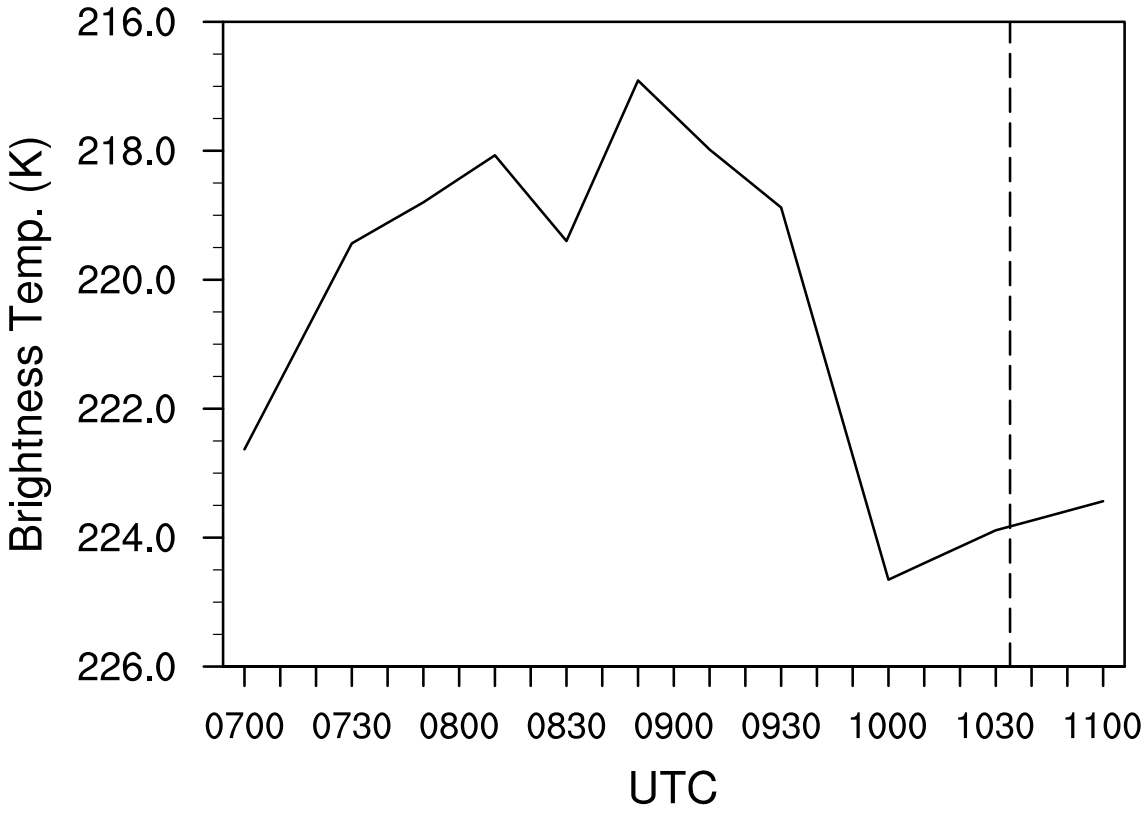

Fig. 3. Time series for the inverse of the minimum brightness temperature (solid line) within the inner boxes in Fig. 2, calculated using the MTSAT data with 20-30 min time intervals.

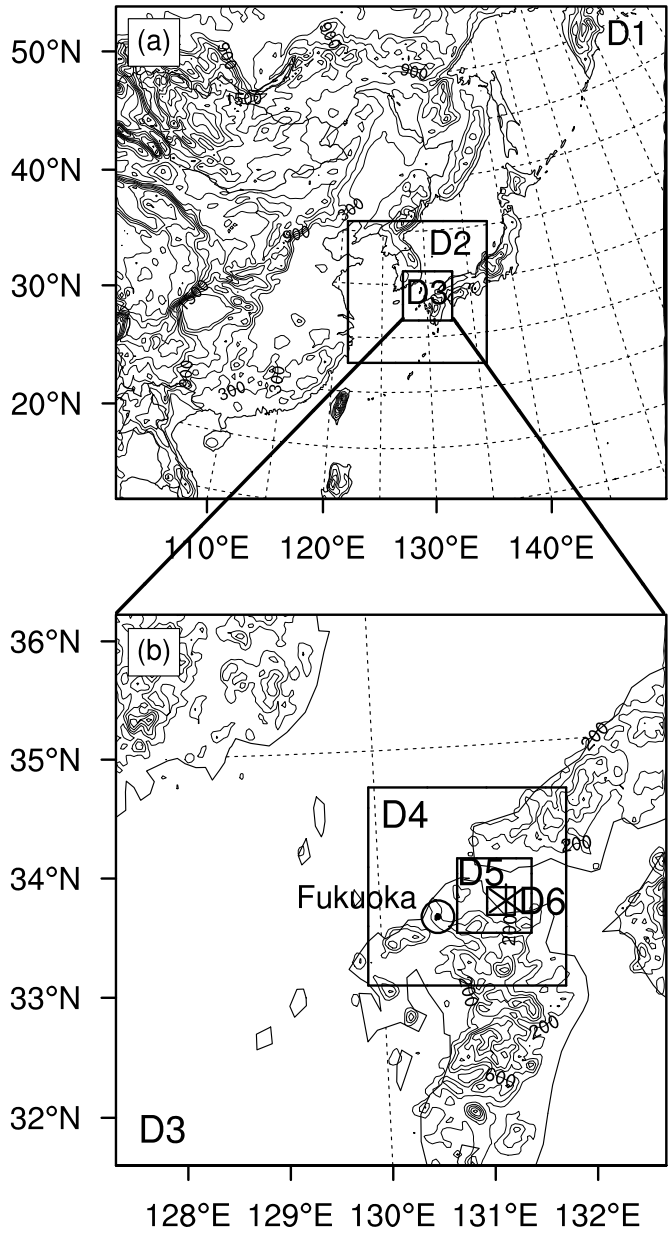

Fig. 4. Horizontal locations of (a) the first three domains (domain 1, Δx = 30 km; domain 2, Δx = 10 km; and domain 3, Δx = 3.3 km) superimposed on the terrain height (m) of domain 1 and (b) the last four domains (domain 3; domain 4, Δx = 1.1 km; domain 5, Δx = 0.37 km; and domain 6, Δx = 0.12 km) superimposed on the terrain height (m) of domain 3. Contour intervals in (a) and (b) are 300 and 200 m, respectively. Location of the turbulence encounter and the radiosonde station at Fukuoka are depicted in (b) as an asterisk and a dot-circle, respectively.

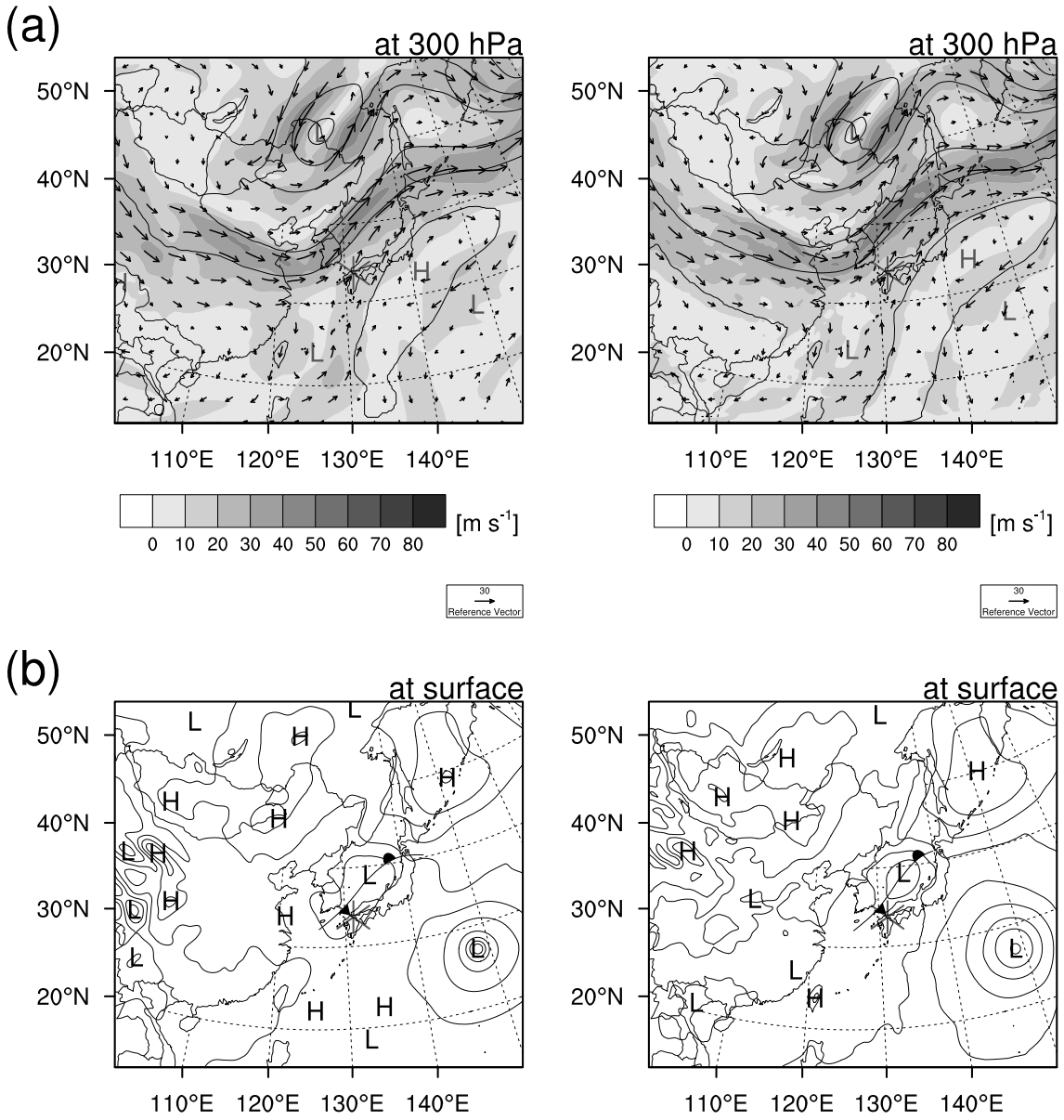

Fig. 5. (a) Geopotential height (contours) superimposed on horizontal wind speed (shading) at 300 hPa and (b) sea-level pressure (contours) at 1200 UTC 2 Sep 2007, obtained from RDAPS 30-km analysis data provided by KMA (left) and WRF model output of domain 1 (right). Contour intervals in (a) and (b) are 60 gpm and 4 hPa, respectively. Location of the turbulence encounter is depicted as an asterisk in all plots.

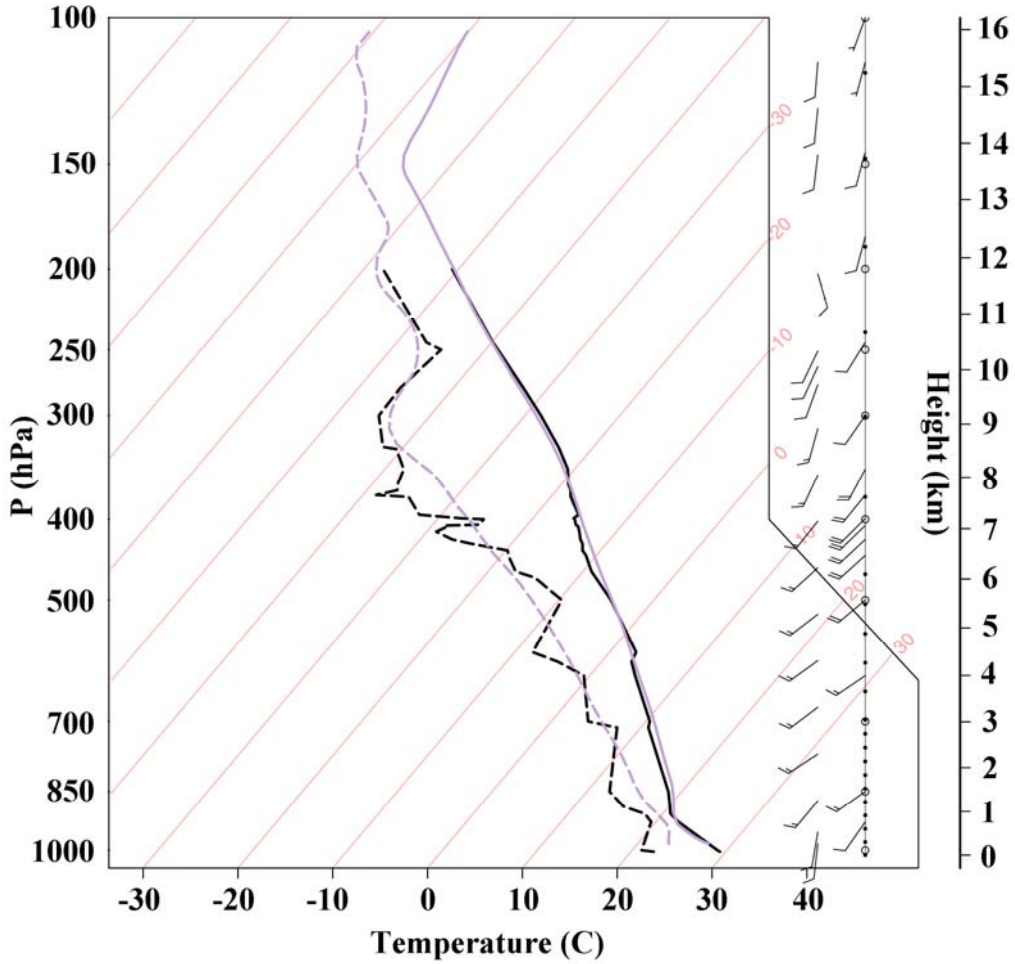

Fig. 6. Skew *T*-log *p* diagrams (solid – temperature, dashed – dew point) obtained from the observed (black) and the simulated (gray) soundings at Fukuoka at 0600 UTC 2 Sep 2007. Simulated (far right) and observed (right) wind speeds at each level are shown on the right side of the diagram with full (10 m s^{-1}) and half (5 m s^{-1}) barbs. Isotherms in 10 ºC intervals are denoted as slantwise thin lines.

(a) **(b)**

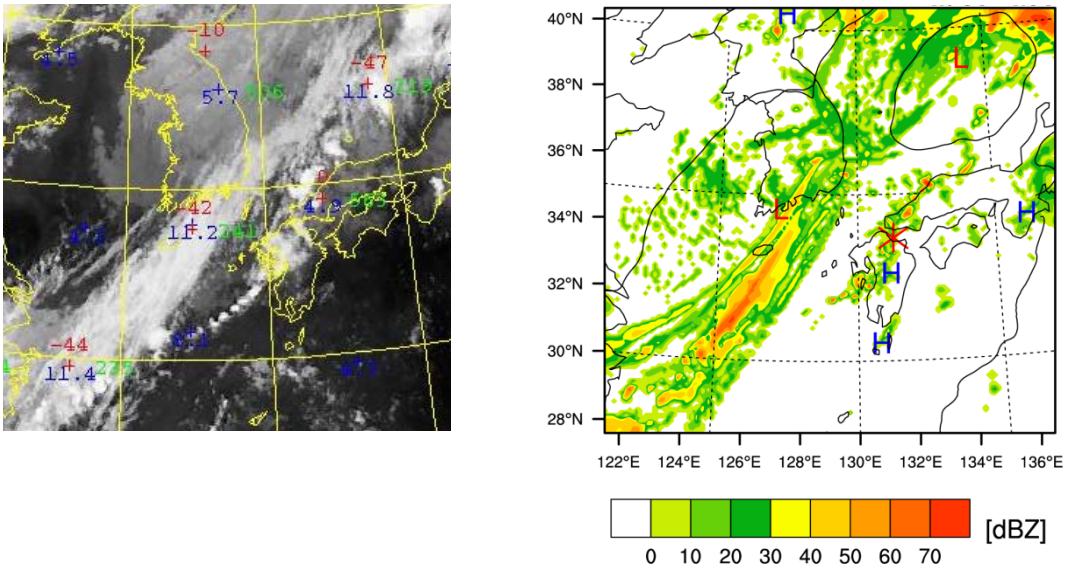

Fig. 7. (a) Composite image obtained from the MTSAT at 1033 UTC and (b) column maximum radar reflectivity (shading) and sea level pressure (contour), derived using the simulated result in domain 2 at 1030 UTC 2 September 2007. Location of the turbulence encounter is depicted as an asterisk in (b).

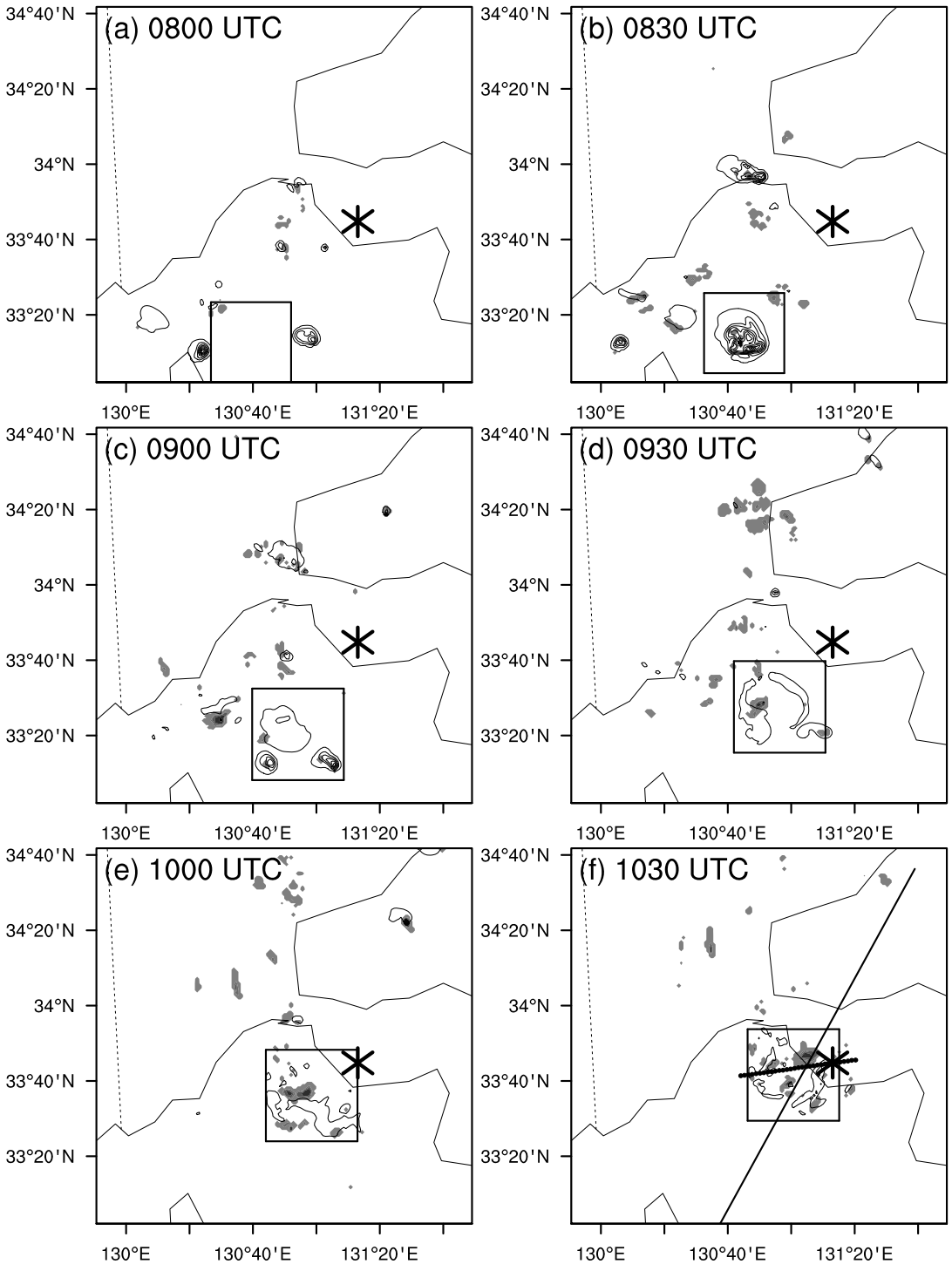

Fig. 8. SGS TKE (> 0.1 m^2 s^{-2}; shading) with total cloud mixing ratio (> 0.1 g kg^{-1}; contours) in domain 4 at z = 11.2 km at (a) 0800, (b) 0830, (c) 0900, (d) 0930, (e) 1000, and (f) 1030 UTC 2 Sep 2007. Location of the turbulence encounter and flight route of the aircraft from 1033 to 1034 UTC are depicted as asterisks in (a-f) and bold line in (f).

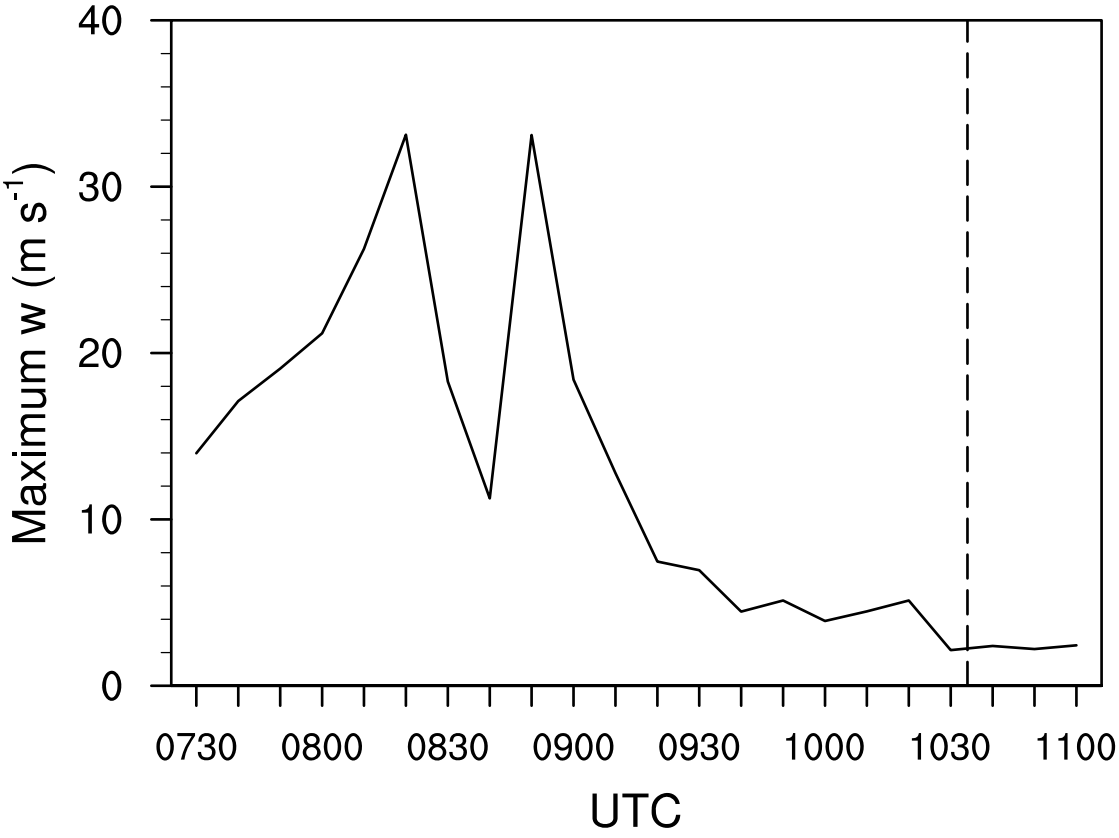

Fig. 9. Time series of the maximum vertical velocity (solid line) within the inner boxes in Fig 8, calculated using the model outputs of domain 4 with 1.1 km horizontal grid spacing and 10 min time intervals. The vertical dashed line indicates the time (1034 UTC) of the turbulence encounter.

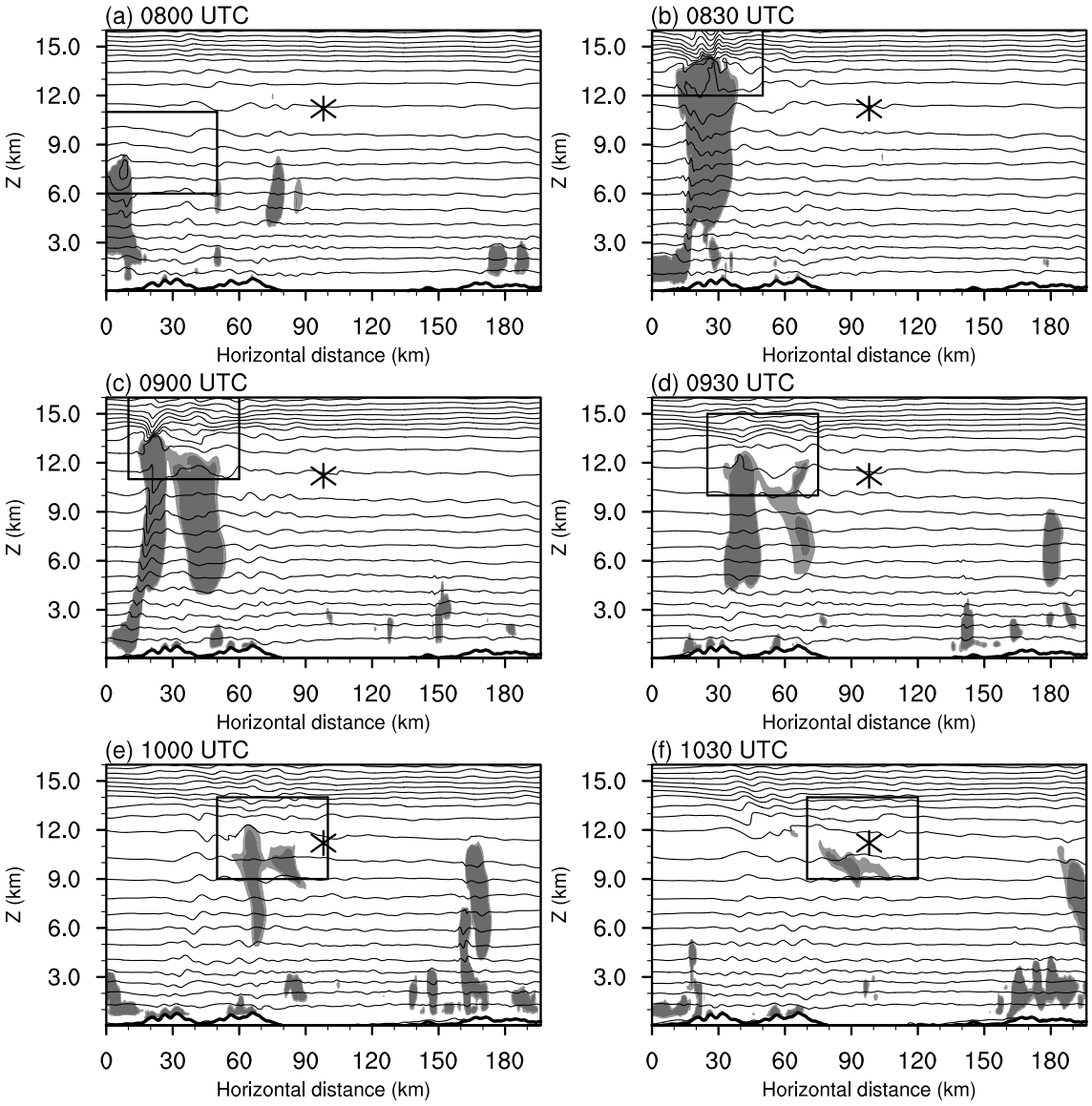

Fig. 10. Vertical cross-sections of total cloud mixing ratio greater than 0.05 g kg^{-1} (light shading) and 0.1 g kg^{-1} (dark shading) with potential temperature (contours) along the solid line in Fig. 8f at (a) 0800, (b) 0830, (c) 0900, (d) 0930, (e) 1000, and (f) 1030 UTC 2 Sep 2007. Contour intervals in all plots are 2 K. Location of the turbulence encounter projected on the cross-sections is depicted as an asterisk in all plots.

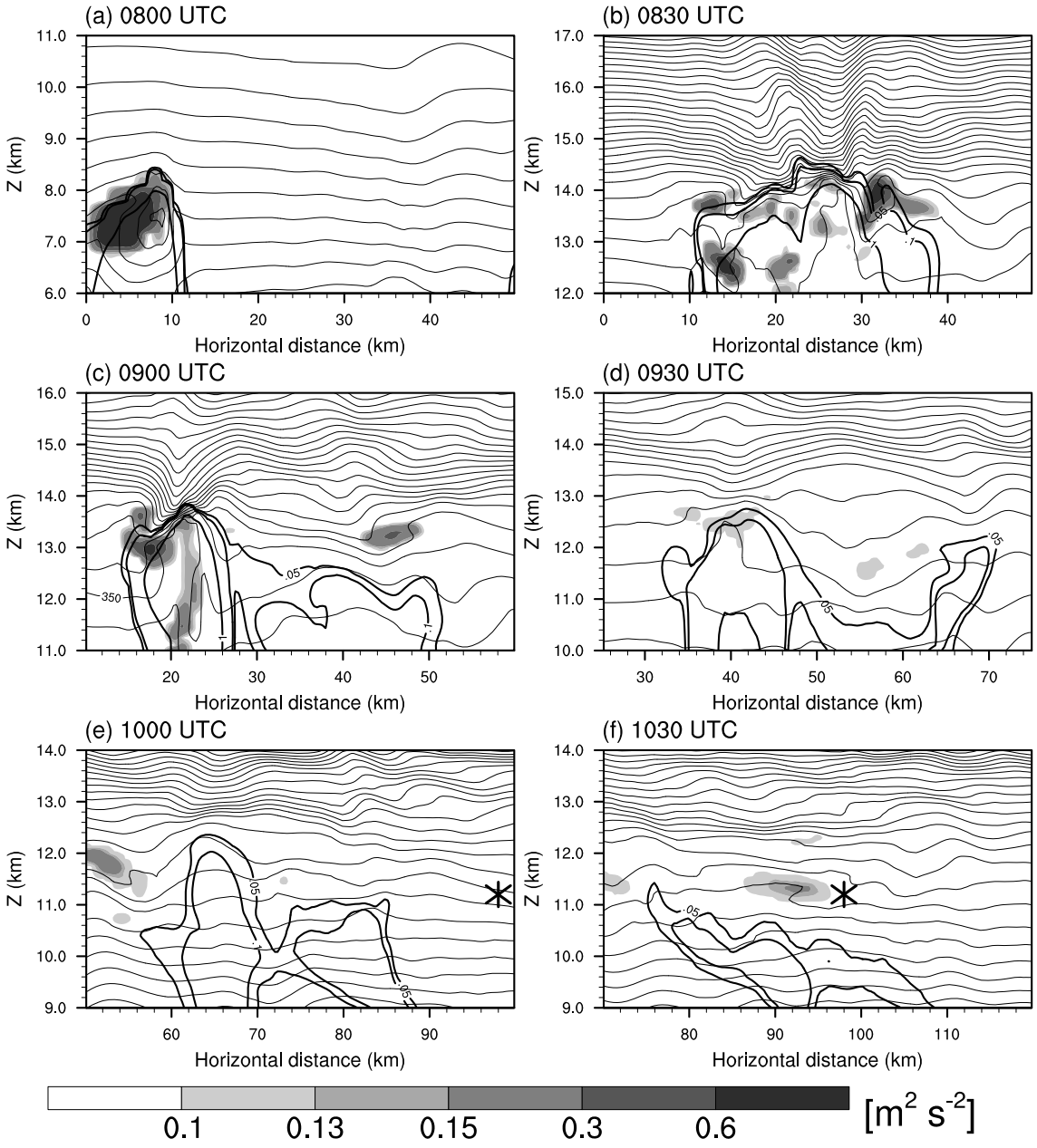

Fig. 11. SGS TKE (shading) with total cloud mixing ratio (0.05, 0.1, and 1 g kg^{-1}; thick lines) and potential temperature (contours) in the inner boxes in Fig. 9 at (a) 0800, (b) 0830, (c) 0900, (d) 0930, (e) 1000, and (f) 1030 UTC 2 Sep 2007. Contour interval is 2 K for plots (a-d) and 1 K for (e) and (f).

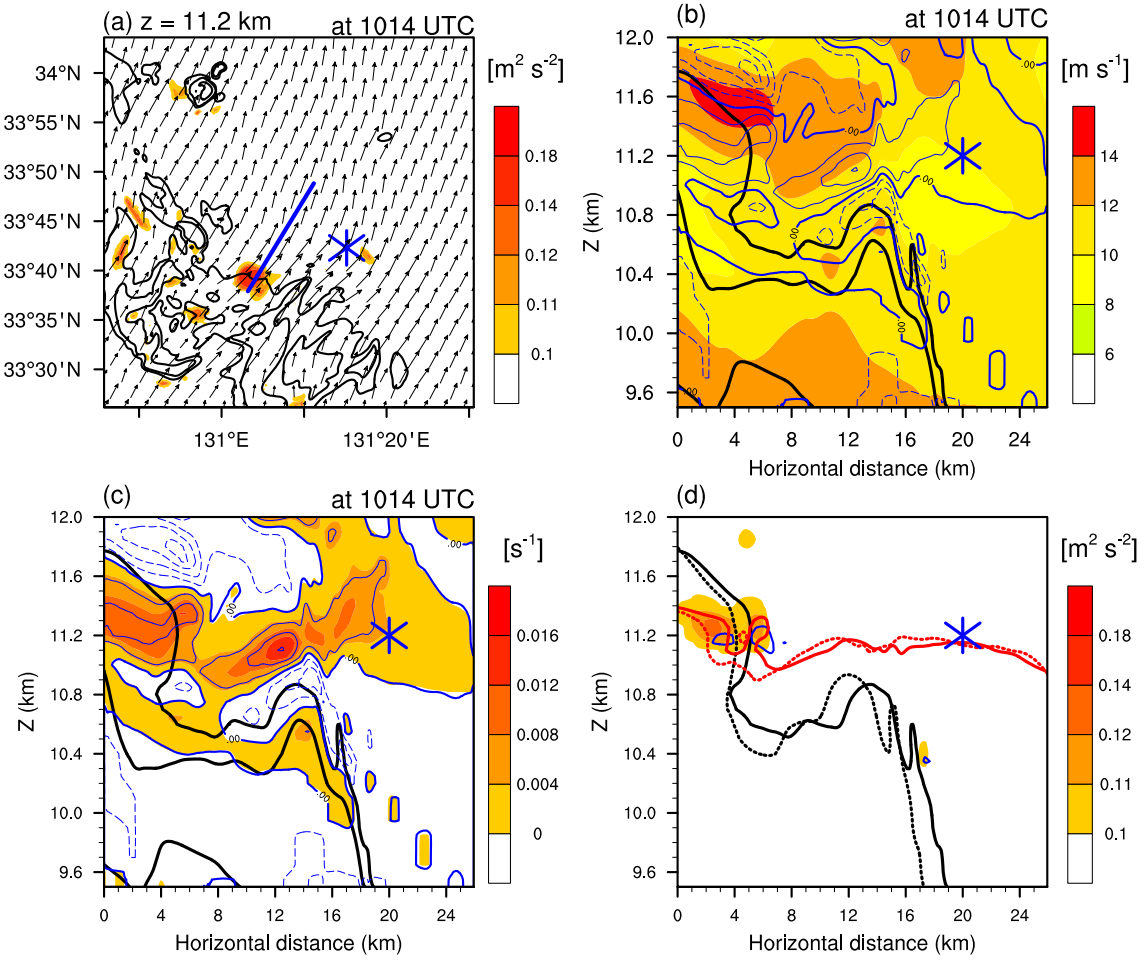

Fig. 12. (a) SGS TKE (shading), total cloud mixing ratio (0.03, 0.1, and 1 g kg^{-1}; solid contours), horizontal wind vectors at z = 11.2 km in domain 5. Vertical cross-sections of (b) horizontal wind speed (shading), (c) $\partial u / \partial z$ (shading), and (d) SGS TKE (shading) along the blue line in (a), using the model results in domain 6 at 1014 UTC 2 Sep 2007. Blue and black contours in (b) and (c) are y-vorticity ($\eta = \partial u / \partial z - \partial w / \partial x$; s^{-1}) and total cloud mixing ratio (0.03 and 0.1 g kg^{-1}), respectively. In (d), the blue contour is zero N^2 at 1014 UTC, and the black and red lines show the total cloud mixing ratio of 0.03 g kg^{-1} and the isentrope of 346 K at 1012 (dashed) and 1014 (solid) UTC, respectively. Zero and negative values in (b) and (c) are bold and dashed lines, respectively. Turbulence location in all plots is indicated by an asterisk.

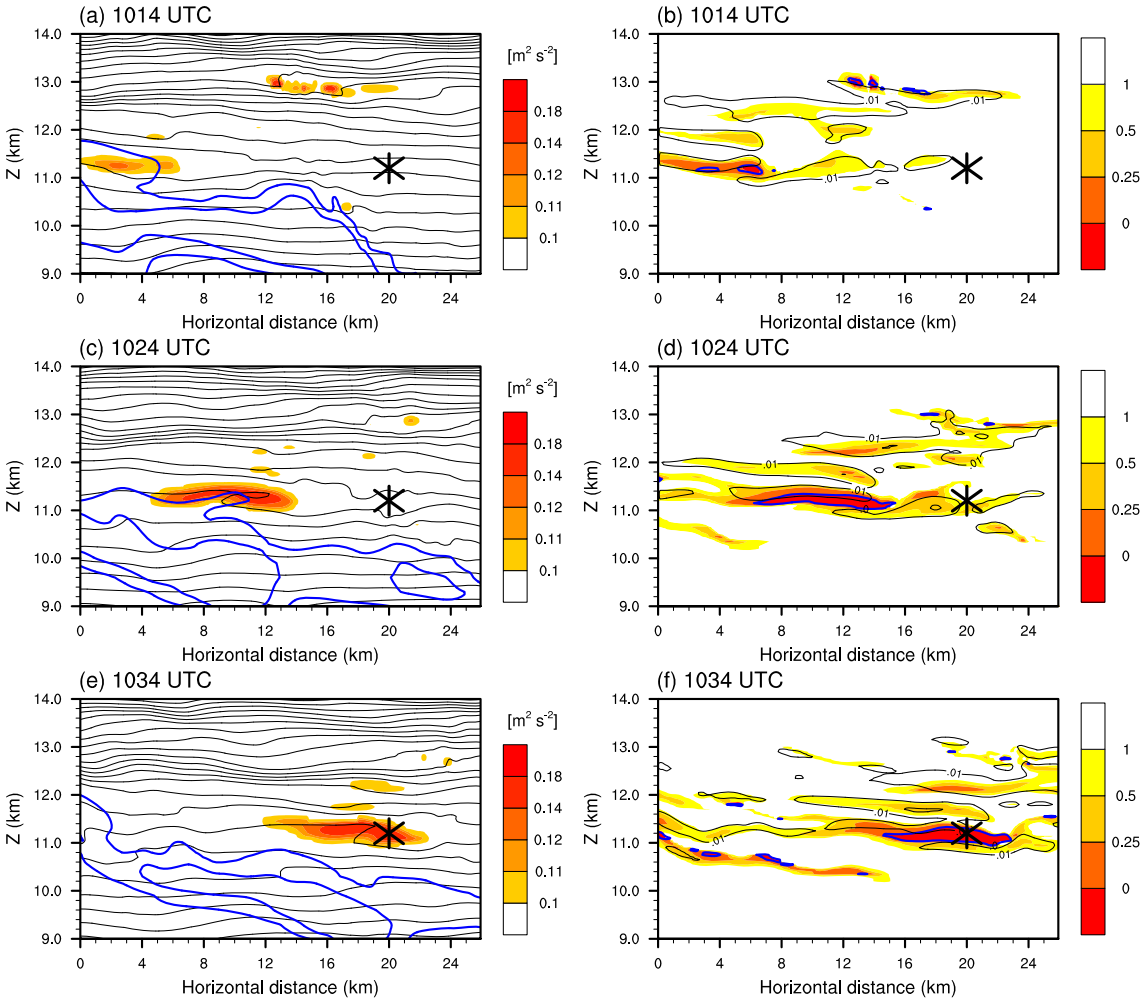

Fig. 13. Vertical cross-sections of SGS TKE (shading) with total cloud mixing ratio (0.03 and 0.1 g kg^{-1}; thick lines) and potential temperature (contours) (left panel) and Richardson number (shading) with zero N^2 (thick line) and VWS (contours) (right panel) along the blue line in Fig. 12a at (a and b) 1014 UTC, (c and d) 1024 UTC, and (e and f) 1034 UTC 2 Sep 2007, calculated using the model results of domain 6. Contour intervals in left and right panels are 2 K and 0.01 s^{-1}, respectively. Turbulence location projected in the cross-section is depicted as an asterisk in all plots.

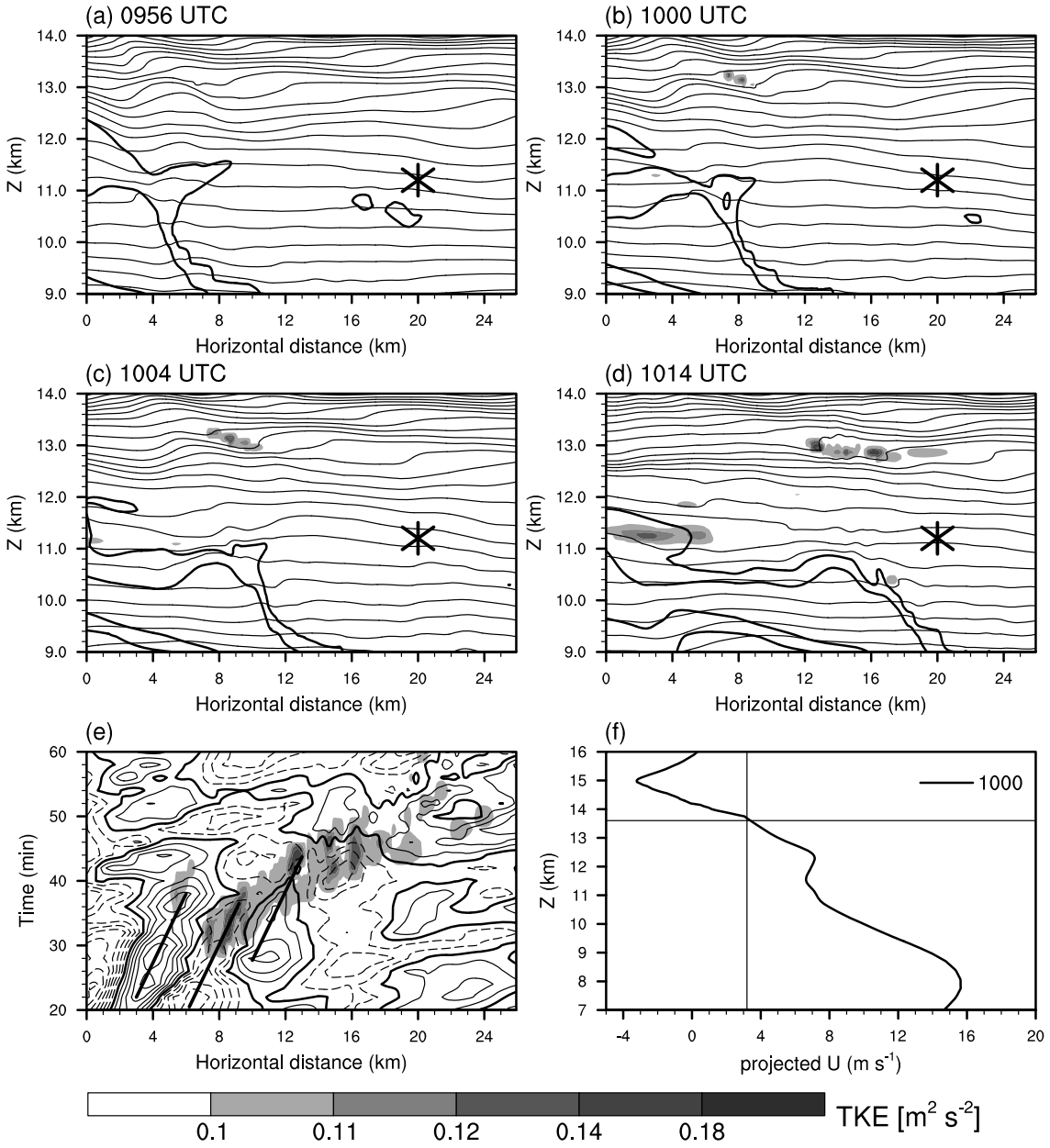

Fig. 14. Panels (a-c) are the same as Fig. 13 (left), except taken at (a) 0956 UTC, (b) 1000 UTC, and (c) 1004 UTC. Panel (d) is the same as Fig. 13a. (e) The temporal evolution (*t*-*x* cross-section) of vertical velocity (m s^{-1}) at z = 12.7 km in (a-d) with vertically averaged SGS TKE (shading) between z = 12.7 and 13.3 km. Y-axis is the time from 0930 UTC, when the gravity waves begin to appear. (f) The vertical profile of zonal-mean horizontal wind speed (U) in (b). Slant lines in (e) and the vertical line in (f) represent a phase speed of 3.2 m s^{-1}, and the horizontal line in (f) is z = 13.6 km.

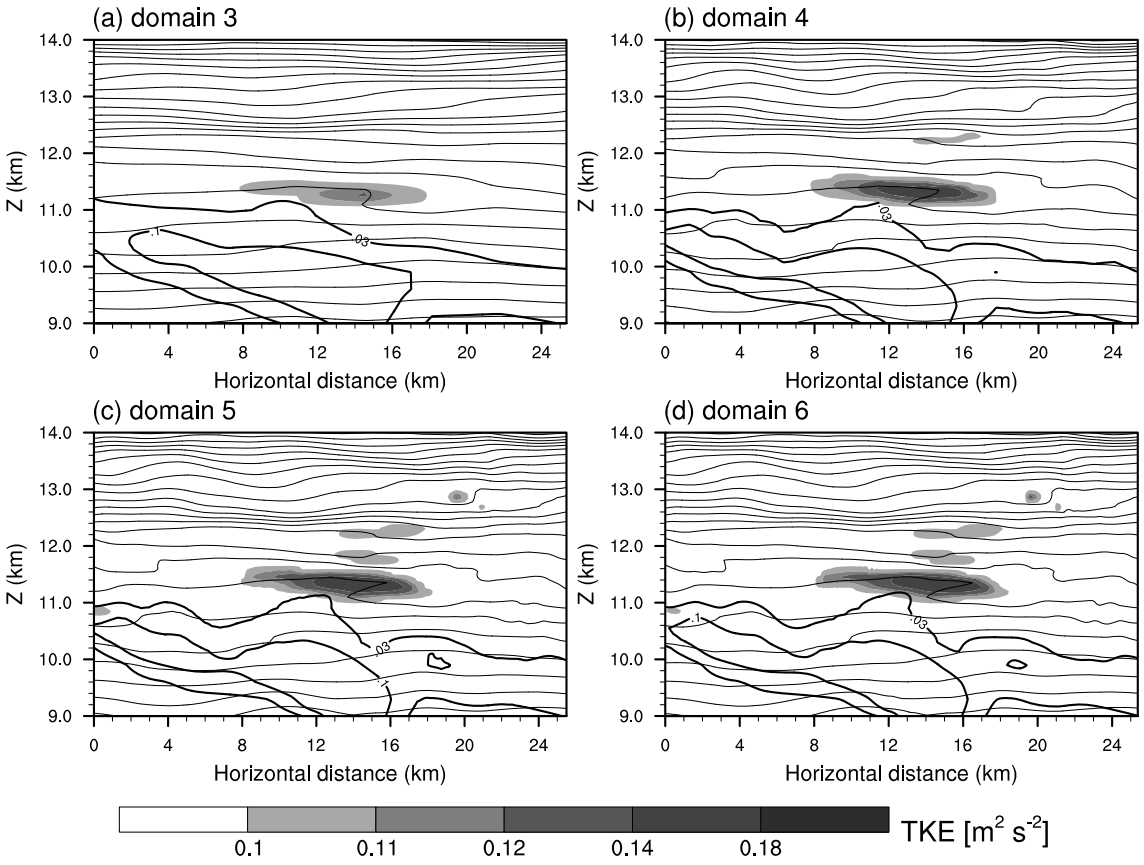

Fig. 15. Vertical cross-sections of SGS TKE (shading) with total cloud mixing ratio (0.03, 0.05, and 0.1 g kg^{-1}; thick lines) and potential temperature (contours) along the thick-solid line in Fig. 8f at 1030 UTC 2 Sep 2007, calculated using the model results of (a) domain 3 (Δx = 3.3 km), (b) domain 4 (Δx = 1.1 km), (c) domain 5 (Δx = 0.37 km), and (d) domain 6 (Δx = 0.12 km).